



Cite this: *Chem. Commun.*, 2025, 61, 10273

Received 31st March 2025,
Accepted 9th June 2025

DOI: 10.1039/d5cc01820j

rsc.li/chemcomm

1 Introduction

KS-DFT, commonly referred to as DFT, is a powerful and widely used computational framework for modeling electronic structure. It has been instrumental in unraveling fundamental

Real-space Kohn–Sham density functional theory for complex energy applications

Zeyi Zhang,^{ab} Liping Liu,^d Drew M. Glenna,^{ac} Asmita Jana,^a Carlos Mora Perez^a and Jin Qian^d ^{*a}

Real-space Kohn–Sham density functional theory (real-space KS-DFT) enables large-scale electronic structure simulations that is particularly well-suited for the modern high-performance computing (HPC) architectures. This feature article reviews its theoretical foundations, highlights the algorithmic advances and recent developments, and showcases applications in complex nano systems. We aim to provide a perspective on the trajectory of real-space KS-DFT as an emerging tool for computational chemistry and materials science in the exascale era.

insights at the atomistic level, which in turn govern macroscopic properties. For a comprehensive review of the theoretical and applied aspects of DFT and its extended electronic structure methods, we refer readers to the paper by Marzari *et al.*¹

When discussing DFT, one's implicit assumption often involves traditional implementations based on either the atomic orbitals or plane-wave basis sets. These methods, as implemented in widely used software packages such as Q-Chem,² Gaussian,³ or VASP,^{4,5} and Quantum Espresso,⁶ have been highly successful but typically scale to systems containing only a few hundred atoms. This limitation arises from the computational cost of solving the KS equations in non-localized

^a Chemical Sciences Division, Lawrence Berkeley National Laboratory, Berkeley, California 94720, USA. E-mail: jqian2@lbl.gov

^b Department of Chemistry, University of California, Berkeley, Berkeley, California 94720, USA

^c Department of Nuclear Engineering & Industrial Management, University of Idaho, Idaho Falls, Idaho 83402, USA

^d Department of Chemical Engineering, Virginia Polytechnic Institute and State University, Blacksburg, Virginia 24060, USA



Zeyi Zhang

Zeyi Zhang received his BS in Chemistry from Shanghai Jiao Tong University in 2022. He is currently a PhD candidate in Chemistry at University of California, Berkeley and a graduate researcher at Lawrence Berkeley National Laboratory under the supervision of Dr Jin Qian and Prof. Martin Head-Gordon. His research mainly focuses on the methodology development of electronic structure theory and its practical applications on various systems from gas phases to condensed phases. Now he is working on the development of real-space DFT and complex-valued molecular orbital methods as well as the theoretical studies of photoionization processes.



Liping Liu

Liping Liu earned his BE in Chemical Engineering from Xi'an Jiao Tong University in 2018 and is currently pursuing his PhD in Chemical Engineering at Virginia Tech under the supervision of Prof. Hongliang Xin. His research integrates quantum-chemical simulations, kinetic modeling, and machine learning to simulate, design, and optimize catalytic materials for sustainable energy and environmental applications. His contributions span single-atom catalysts, metal oxide catalysts, and metal alloy catalysts. Recently, he did an internship at Lawrence Berkeley National Laboratory under the guidance of Dr Jin Qian, working on the development of real-space pseudopotential methods for the calculations of third-row elements X-ray photoelectron spectroscopic signatures.



bases, where the Hamiltonian matrix is dense and diagonalization becomes a bottleneck.

To address the growing need for simulating increasingly complex chemical systems – such as gas–liquid–solid interfaces and large-scale nanostructures (*e.g.*, from ~ 100 to $\sim 10\,000$ atoms), we introduce the latest advances in real-space KS-DFT. Unlike conventional approaches, real-space KS-DFT discretizes the KS Hamiltonian directly on finite-difference (FD) grids in real, physical space.^{7,8} This results in a large but highly sparse eigenproblem matrix, enabling massive parallelization with minimal communication overhead, making real-space KS-DFT particularly well-suited for the modern HPC architectures.

In recent years, several computational breakthroughs have demonstrated the scalability and efficiency of real-space KS-DFT. The PARSEC team⁹ successfully simulated a 20 nm

spherical Si nanocluster containing over 200 000 atoms, solving the electronic structure problem in parallel across 8192 nodes.¹⁰ The ARES team performed extensive benchmarking studies, demonstrating the accuracy of real-space KS-DFT for metallic, semiconductor, and insulating systems directly by comparing the results against CASTEP,¹¹ and also showcased a demonstration of simulating aluminum systems with 10 000 atoms for scalability.¹² The RESCU team has simulated Si and Al systems containing thousands of atoms.¹³ The OCTOPUS team has contributed significantly to time-dependent developments and applications.^{14,15} The SPARC team enabled not only static but also dynamic solutions,^{16,17} while the DFT-FE team developed an all-electron (AE) solution projected on a finite-element (FE) basis.^{18,19}

Despite these achievements, real-space KS-DFT is still in a developmental stage, with most of its applications focused on



Drew M. Glenna

Drew M. Glenna received his BS from the University of Minnesota-Duluth in 2020 and his MS from the University of Idaho in 2024. He is currently a PhD Candidate at the University of Idaho under the guidance of Prof. Haiyan Zhao and is mentored by Dr Jin Qian as a Department of Energy Office of Science Graduate Student Research Program Fellow at Lawrence Berkeley National Laboratory. His research focuses on computational modeling of interfacial phenomena

– specifically adsorption, charge recombination, and charge transfer – to advance clean energy and decarbonization technologies.



Asmita Jana

Asmita Jana received BTech and an MTech in Metallurgical and Materials Engineering from the Indian Institute of Technology Madras (2017). She obtained a PhD in Materials Science and Engineering from the Massachusetts Institute of Technology (2022). She is a postdoctoral researcher at Lawrence Berkeley National Laboratory working on computational modeling for sustainable energy applications. Her research interests are modeling interfacial phenomena

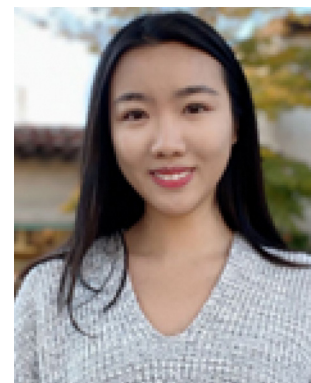
including adsorption, reaction, and transport in electrocatalysts for CO_2 reduction, CO_2 adsorbents, and separations. She is also interested in modeling complex heterogeneous carbon architectures often used in the energy sector.



Carlos Mora Perez

Carlos Mora Perez received his BS in chemistry from California State University, San Bernardino (2015) and his MS from California State Polytechnic University, Pomona (2018). He then received his PhD in chemistry from the University of Southern California (2024) under Prof. Oleg Prezhdo. He is a postdoctoral researcher at Lawrence Berkeley National Laboratory, working on computational modeling for ultrafast time-domain science. His research focuses on nonadiabatic

molecular dynamics (NAMD) simulations to explore exciton behavior and related photophysical processes, including charge and energy transfer, exciton dissociation, and charge recombination.



Jin Qian

Jin Qian is an early-career staff scientist at Lawrence Berkeley National Laboratory. She earned her PhD degree from California Institute of Technology with Prof. William Goddard in 2019 and established her research group at Berkeley Lab in 2021. Her research focuses on computational chemistry and materials science via (1) developing digital twins to bridge theory and experiment, and (2) advancing real-space KS-DFT for large-scale electronic structure

simulations. A recipient of the DOE Early Career Award, she integrates HPC to study ultrafast excited-state dynamics and complex gas–liquid–solid interfaces, pushing the boundaries of first-principles simulations for chemistry and materials science.

model systems.^{8,10,20–22} In computational chemistry and materials science, practical demonstrations of its advantages remain limited, and further benchmarks are needed for spectroscopic validation and comparison with experimental observables.^{23–26}

In this article, we introduce the theoretical foundations and algorithmic innovations of real-space KS-DFT. We first review key theoretical background, including the KS equation, pseudopotentials (PPs), and FD discretization. Then we discuss computational acceleration techniques such as subspace filtering,^{27,28} Rayleigh–Ritz diagonalization,²⁹ and space-filling curves for parallelization.³⁰ To bridge the gap between theory and experiments, we developed a PP based method within the real-space KS-DFT framework to predict X-ray photoelectron spectroscopy (XPS) core electron binding energy (CEBE).^{24,26} Following this, we discuss recent applications from our group, including studies on complex nanodroplet interactions with gas-phase species and carbon capture near the direct air capture (DAC) limit. These examples illustrate cases where real-space KS-DFT provides unique insights as well as instances where conventional DFT remains sufficient, respectively. For completeness, alternative methods for simulating large systems, such as orbital-free DFT (OF-DFT) and linear scaling DFT, are also reviewed. Finally, we provide an outlook on the future of real-space KS-DFT, emphasizing its potential for exascale computing and its evolving role in computational materials science and chemistry. Current *status quo*, challenges and gaps, along with potential solutions, are summarized in this section, in detail. By evaluating both its strengths and limitations, we aim to provide a clear perspective on the trajectory of real-space KS-DFT as an emerging computational tool in chemistry and materials science.

2 Theory

2.1 KS equation

Real-space KS-DFT is fundamentally based on the KS equation:^{31,32}

$$\hat{H}\psi_i(\vec{r}) = \left\{ -\frac{1}{2}\nabla^2 + V[\rho(\vec{r}), \vec{r}] \right\} \psi_i(\vec{r}) = E_i \psi_i(\vec{r}) \quad i = 1, 2, \dots \quad (1)$$

where atomic units ($\hbar = m_e = e = 4\pi\epsilon_0 = 1$) are used and will be used throughout the entire manuscript. $\psi_i(\vec{r})$ is the wavefunction or eigenfunction, E_i is the energy or eigenvalue, and \vec{r} is the position. $\rho(\vec{r})$ represents the charge density and is defined as:

$$\rho(\vec{r}) = \sum_{i=1}^{n_{\text{occ}}} f_i |\psi_i(\vec{r})|^2 \quad (2)$$

where n_{occ} is the number of occupied states, f_i is the number of electrons in the occupied state. The potential V in the Hamiltonian can be written as:

$$V[\rho(\vec{r}), \vec{r}] = V_{\text{H}}[\rho(\vec{r})] + V_{\text{ion}}(\vec{r}) + V_{\text{xc}}[\rho(\vec{r})] \quad (3)$$

where V_{H} is the Hartree or Coulomb potential, which is calculated through the Poisson equation:

$$\nabla^2 V_{\text{H}}[\rho(\vec{r})] = -4\pi\rho(\vec{r}) \quad (4)$$

V_{ion} is the ionic potential, and V_{xc} is the exchange–correlation potential, which can be approximated by local density approximation (LDA),³² generalized gradient approximation (GGA),³³ other LDA/GGA variants,^{34–37} or higher rungs in the Jacob's ladder.³⁸ After solving the KS equation self-consistently, we obtain the KS orbitals, which give the charge density, where additional properties can then be derived. The standard scaling for KS-DFT calculation is $\mathcal{O}(N_{\text{a}}^3)$ for GGA, where N_{a} is the number of atoms.^{1,39}

2.2 PP theory

In most practical electronic structure calculations, the PP approach is preferred over the AE methods due to its substantial computational advantages. By replacing the strong Coulomb potential of the nucleus and tightly bound core electrons with a smoother effective potential, PPs eliminate the need to resolve the rapidly oscillating core wavefunctions, which require extremely fine grids or large basis sets. Since core electrons are usually chemically inert, this approximation introduces little loss in accuracy for most materials properties. As a result, PPs significantly reduce the computational cost and improve numerical stability. Consequently, we choose to introduce real-space KS-DFT in this article with a particular focus on the FDPP approach.

2.2.1 Phillips–Kleinman cancellation theorem. The ionic potential V_{ion} , also called ionic core pseudopotential, in eqn (3) is approximated by PPs in the present real-space KS-DFT theoretical framework. The PP concept was first proposed based on the observation that core electrons are localized and inert while valence electrons are delocalized and active.⁴⁰ Later, it was found that the strong ionic core potential could be replaced by a weak PP,⁴¹ and a cancellation theorem was then developed.⁴² This theorem simplifies the AE problem into a PP problem in which only valence electrons are solved explicitly.

We show the basic idea here. For an atom, we assume one valence wavefunction can be replaced by a pseudo-wavefunction and core wavefunctions:

$$|\psi_v\rangle = |\phi_p\rangle - \sum_c^{\text{cores}} |\psi_c\rangle \langle \psi_c | \phi_p \rangle \quad (5)$$

where ψ_c , ψ_v and ϕ_p represent core, valence, and pseudo-wavefunctions. The coefficient $\langle \psi_c | \phi_p \rangle$ comes from orthonormality. Suppose E_c , E_v , and E_p are eigenvalues of corresponding wavefunctions. Substituting eqn (5) into eqn (1), we obtain

$$\underbrace{\left[\hat{H} + \sum_c^{\text{cores}} (E_v - E_c) |\psi_c\rangle \langle \psi_c | \right] | \phi_p \rangle}_{\hat{V}_R} = E_v |\phi_p\rangle \quad (6)$$

where \hat{H}_p is a newly defined pseudo-Hamiltonian, and \hat{V}_R is the repulsive potential energy operator. Incidentally, a PP is obtained:

$$V_p |\phi_p\rangle = (V + V_R) |\phi_p\rangle \quad (7)$$

where V is the AE potential and V_R is a repulsive potential. This details the cancellation theorem.

In principle, if we were able to solve eqn (6), the pseudo-wavefunction and PP can be obtained. However, \hat{V}_R is a non-local operator which has a dependency on E_v , resulting in an energy-dependent Hamiltonian that is impractical to solve. Therefore, in practice, PPs are not solved from this theorem but are constructed from the KS equation, as discussed below.

2.2.2 Construction of PPs. To construct well-behaved pseudo-wavefunctions, the following requirements are usually applied:^{43,44}

(1) The eigenvalue for ϕ_p should be identical to ψ_v with $E_p = E_v$;
 (2) Pseudo-wavefunctions should be nodeless, leading to $\phi_p > 0$;

(3) The pseudo-wavefunction should be equal to the AE wavefunction beyond a chosen core radius r_c , that is $\phi_p = \psi_v$, when $r > r_c$.

Based on (3), if ϕ_p is normalized, the corresponding PP is said to be “norm-conserving (NC)”, which encloses the same charge density within the core region: $\int_0^{r_c} |\phi_p|^2 d\vec{r} = \int_0^{r_c} |\psi_v|^2 d\vec{r}$.

There are PPs that do not meet the NC condition, such as ultrasoft PPs⁴⁵ and PAW.⁴⁶ However, in the FDPP method, NC-PPs are commonly used, especially through the Martins-Troullier form of pseudo-wavefunctions:^{44,47}

$$\phi_p(r) = \begin{cases} r^l \exp[p(r)], & r \leq r_c \\ \psi_v(r), & r > r_c \end{cases} \quad p(r) = \sum_{i=0}^6 c_{2i} r^{2i} \quad (8)$$

where c_{2i} are coefficients determined by forcing the NC condition and the continuity for ϕ_p and its first four derivatives at r_c . PPs are then obtained by inverting eqn (1):

$$V_{\text{ion},p,i}(r) = E_i - V_H[\rho(r)] - V_{\text{xc}}[\rho(r)] + \frac{\hbar^2 \nabla^2 \phi_{p,i}}{2m\phi_{p,i}} \quad (9)$$

The index i in the expression indicates the state-dependent character, which means that PPs are different for s-, p-, and d-electrons in different shells.

2.2.3 Nonlocality. After obtaining the atomic pseudo-wavefunctions and PPs, we construct the total ionic PP energy operator. This operator $\hat{V}_{\text{ion},p}^{\text{tot}}$, which describes the interactions between valence electrons and pseudo-ionic cores in the system, can then be separated into a local part and a nonlocal part:⁴⁸

$$\hat{V}_{\text{ion},p}^{\text{tot}}(\vec{r}) = \sum_a \hat{V}_{\text{loc},p}^a(r_a) + \sum_{a,lm} \frac{\langle \Delta \hat{V}_{p,l}^a(r_a) \phi_{p,lm}^a(r_a) \rangle \langle \phi_{p,lm}^a(r_a) \Delta \hat{V}_{p,l}^a(r_a) \rangle}{\langle \phi_{p,lm}^a(r_a) | \Delta \hat{V}_{p,l}^a(r_a) | \phi_{p,lm}^a(r_a) \rangle} \quad (10)$$

$$r_a = |\vec{r} - \vec{R}_a| \quad \Delta \hat{V}_{p,l}^a(r) = \hat{V}_{p,l}^a(r) - \hat{V}_{\text{loc},p}^a(r)$$

$$\hat{V}_{p,l}^a(r) = \hat{V}_{\text{loc},p}^a(r) = \hat{V}_{\text{ion}} \text{ for } r > r_c$$

where a labels the atom in the system and \vec{R}_a is the nucleus position of it. $\phi_{p,lm}^a$ is the pseudo-wavefunction corresponding to

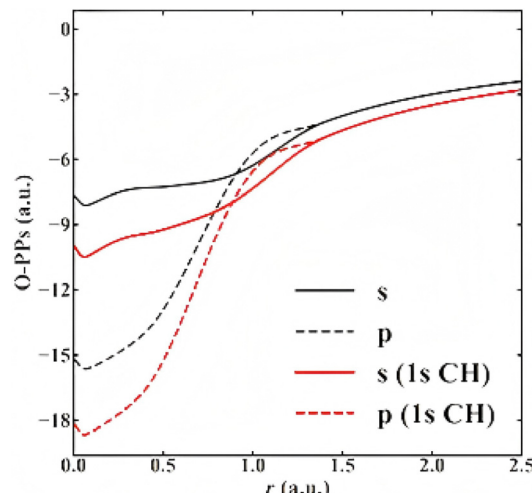


Fig. 1 An illustration of PPs for s and p orbitals for O atom and O1s1 atom. Red lines are PPs for the first shell, and black lines are PPs for the second shell. Figure is reproduced with permission from ref. 24 under a Creative Commons License CC BY 4.0.

the angular momentum number l,m for the a -th atom. $V_{p,l}^a$ is the PP generated by eqn (9), whereas $V_{\text{loc},p}^a$ is the local PP part of $V_{p,l}^a$'s. In practice, the choice of the local part can be arbitrary. For example, choosing either the 2s or 2p as the local PP is allowed for 2nd row elements. If 2p is selected as the local PP, then the 2p component must be subtracted from the 2s component when constructing the nonlocal potential. It is often convenient to use the highest l -component of interest, which simplifies the projection operators. To improve upon the accuracy, this choice can be tested by benchmarking the results from different components and assessing the overall solutions. However, two things need to be emphasized. First, all PPs outside the core region are the same, which are set to the real AE V_{ion} . This indicates that there is no nonlocal contribution outside the core region, meaning the nonlocal potential is a short-range interaction. Second, the summation of l,m should be interpreted as the inclusion of all valence orbitals. Fig. 1 shows an example of PPs for the O atom and O1s1 atom, meaning that one 1s core-hole (CH) is created for XPS. The cancellation of the strong potential in the core region can be seen from the shape of the lines. Instead of a $-Z_{\text{eff}}/r$ -shape curve (Z_{eff} is the effective core charge imposed on an electron), the PPs go to some finite values at $r = 0$, showing a weak potential character. The nonlocality can be recognized by the fact that, within the same shell, different subshells have different PPs (as seen by the differences between the red and black lines in Fig. 1).

2.3 FD method

The FD method lies at the heart of the real-space DFT framework. Instead of relying on the atomic or plane-wave basis set, real-space KS-DFT represents the Hamiltonian matrix in terms of grids in real space. We can write the 3D Laplacian, which is the kinetic part of the Hamiltonian, in terms of wave function



values at these FD grids:^{7,8}

$$\begin{aligned} \nabla^2 f(x_i, y_j, z_k) = & \frac{1}{h^2} \left[\sum_{n_x=-N}^N C_{n_x} f(x_i + n_x h, y_j, z_k) \right. \\ & + \sum_{n_y=-N}^N C_{n_y} f(x_i, y_j + n_y h, z_k) \\ & \left. + \sum_{n_z=-N}^N C_{n_z} f(x_i, y_j, z_k + n_z h) \right] + \mathcal{O}(h^{2N}) \end{aligned} \quad (11)$$

where h is the grid spacing, N is the order of terms expanded, C_{n_x} , C_{n_y} , and C_{n_z} are the coefficients corresponding to the expanded terms, and the Laplacian is expanded based on the grid (x_i, y_j, z_k) . The expansion coefficients for the FD expressions up to $N = 5$ are given in Table 1. Generally speaking, real-space grids do not have to be uniform, but uniform grids are commonly used due to their simplicity and compatibility with FD stencils. Non-uniform or adaptive grids^{50,51} can offer greater efficiency by providing higher resolution near nuclei or regions with rapid variation, while using coarser spacing elsewhere. Such approaches are particularly useful in systems with strong spatial inhomogeneity. In addition, the computational complexity of the real-space calculation increases cubically with the number of grid points, meaning the user should choose a modest N and a coarser h that still satisfies the desired energy convergence criteria.

For isolated or non-periodic cases, we need to specify a cutoff radius R_{cut} that contains the entire system and is large enough to capture the accurate electron density. The wavefunction values are forced to be zero outside the domain defined by R_{cut} . This is called Dirichlet boundary condition (DBC). A typical geometry for a FD domain with DBC is illustrated in Fig. 2.

With these FD grids as a “basis set”, we can now analyze the sparsity of the discretized Hamiltonian matrix. For the kinetic energy component, it is a near-diagonal matrix, and the width of the diagonal nonzero lines will depend on the order of expansion. For the potential energy component, the V_{H} and V_{xc} matrices are strictly diagonal because of the locality. As for the V_{ion} part, the local term is diagonal, and the nonlocal terms will only be nonzero around the core region for each atom due to the short-range character. Therefore, the relatively small width (usually with an expansion order $N = 12\text{--}15$) of nonzero diagonal elements in the kinetic matrix compared to the high dimension of the total matrix, the locality of V_{H} , V_{xc} , $V_{\text{loc,p}}$, and the short-range character of the nonlocal ionic PP lead to a

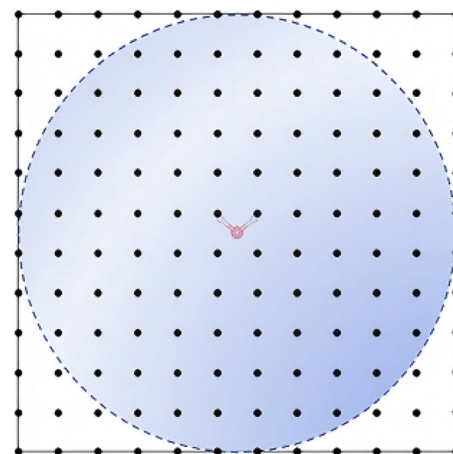


Fig. 2 An example for the real-space grids representation, where R_{cut} is shown by the blue sphere. The wave function is set to zero outside the sphere. Figure is reproduced with permission from ref. 24 under a Creative Commons License CC BY 4.0.

sparse Hamiltonian matrix. An example of the Hamiltonian sparsity analysis for CH_4 is illustrated in Fig. 3. Here, we set $N = 8$, and $h = 0.4$ a.u. as an example. The darker near-diagonal elements correspond to the Laplacian, and the light off-diagonal elements come from the nonlocal ionic PP contribution. The cutoff is set to 10^{-7} a.u. One can anticipate that lower thresholds will give even sparser matrix form.

2.4 Algorithmic considerations

2.4.1 Subspace filtering. The Hamiltonian matrix expressed in grid values has a large dimension (typically $10^6 \times 10^6$), especially when R_{cut} is large and h is small. Consequently, a great amount of computational time is consumed for the diagonalization steps. However, not all eigenvalues are of interest, and only the occupied states and a handful of virtual states are usually needed. A clever approach is to filter out unwanted dimensions of the matrix using subspace projection techniques.

Suppose we have the following set of grids-based wavefunctions:

$$\Psi = \begin{bmatrix} \psi_1(\vec{r}_1) & \psi_2(\vec{r}_1) & \cdots & \psi_m(\vec{r}_1) \\ \psi_1(\vec{r}_2) & \psi_2(\vec{r}_2) & \cdots & \psi_m(\vec{r}_2) \\ \cdots & \cdots & \cdots & \cdots \\ \psi_1(\vec{r}_N) & \psi_2(\vec{r}_N) & \cdots & \psi_m(\vec{r}_N) \end{bmatrix} := [\psi_1, \psi_2, \dots, \psi_m] \quad (12)$$

where $\psi_j(\vec{r}_k)$ is the wavefunction value for the j -th eigenvalue at the grid point r_k , and N is the number of grids in the domain. We can then construct a projection operator using a Hamiltonian form of polynomials and apply it to one column of wavefunctions:

$$\mathcal{P}(H)\psi_1 = \left(\sum_{n=1}^M a_n H^n \right) \psi_1 = \left(\sum_{n=1}^M a_n E_1^n \right) \psi_1 = \mathcal{P}(E_1)\psi_1 \quad (13)$$

If the factor $\mathcal{P}(E_1)$ is close to zero for eigenvalues above a specific state and stays large for the remaining ones, we then “filter out” the components that have higher energies and only

Table 1 Expansion coefficients for FD expressions⁴⁹

Order	C_0	$C_{\pm 1}$	$C_{\pm 2}$	$C_{\pm 3}$	$C_{\pm 4}$	$C_{\pm 5}$
$N = 1$	-2	1				
$N = 2$	-5/2	4/3	-1/12			
$N = 3$	-49/18	3/2	-3/20	1/90		
$N = 4$	-205/72	8/5	-1/5	8/315	-1/560	
$N = 5$	-5269/1800	5/3	-5/21	5/126	-5/1008	1/3150



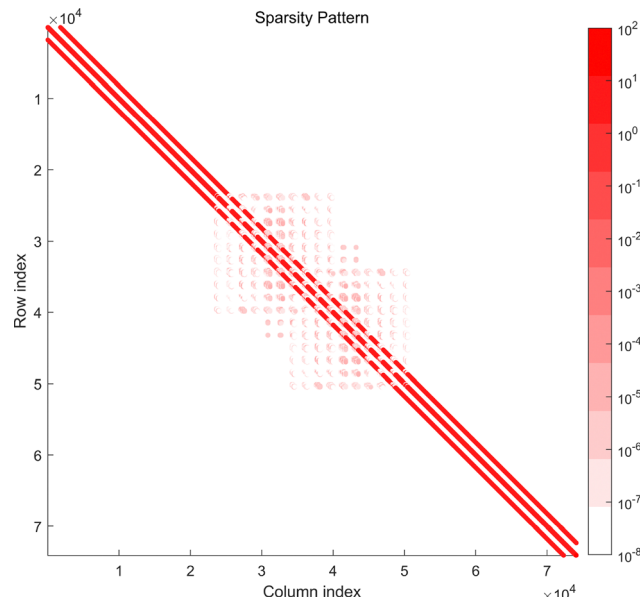


Fig. 3 An example illustrating the Hamiltonian sparsity using CH_4 as an example (left). Different gradient of red is used to indicate the value of the matrix elements, with darker color corresponding to non-zero values and lighter color corresponding to near-zero terms (right). [This analysis is based on the Hamiltonian matrix generated by the Matlab version of the PARSEC code. The coordinates (in a.u.) for atoms are $\text{C}(0, 0, 0)$, $\text{H}(1.2, 1.2, 1.2)$, $\text{H}(1.2, 1.2, -1.2)$, $\text{H}(1.2, -1.2, -1.2)$, $\text{H}(-1.2, 1.2, -1.2)$, and other critical settings (such as N , h , cutoff) are the default values from the code].

keep the states we are interested in. An ideal design for such a polynomial is shown in Fig. 4.

A very common and popular choice that satisfies the requirement mentioned above is called the Chebyshev polynomials:^{9,27,28}

$$\begin{aligned} P_0(x) &= 1 & P_1(x) &= x \\ P_{n+1}(x) &= 2xP_n(x) - P_{n-1}(x) & n \geq 0 \end{aligned} \quad (14)$$

The Chebyshev polynomials stay close to zero within $[-1, 1]$ while having large values outside $[-1, 1]$, and these polynomials are easy to expand to higher orders by the recursion relation.

The next step is to map the unwanted states in the energy spectrum to the range $[-1, 1]$. Suppose that the full spectrum of the Hamiltonian H , denoted as $\sigma(H)$, spans within $[a_0, b]$, and we only want the states in the range $[a_0, a]$ ($a_0 < a < b$). So, we need to map $[a, b]$ to $[-1, 1]$ by:

$$\Psi' = \mathcal{P}\left(\frac{H - c}{e}\right)\Psi, \quad c = \frac{a + b}{2}, \quad e = \frac{b - a}{2} \quad (15)$$

In practice, the lower bound a is obtained from a previous iteration, and the upper bound b is estimated using 4 or 5 Lanczos steps.⁵²

2.4.2 Orthonormalization. After the subspace filtering step, we arrive at a new set of wavefunctions that contain only the states we care about. Since the Chebyshev subspace filtering is not necessarily a unitary transformation, we need to orthonormalize

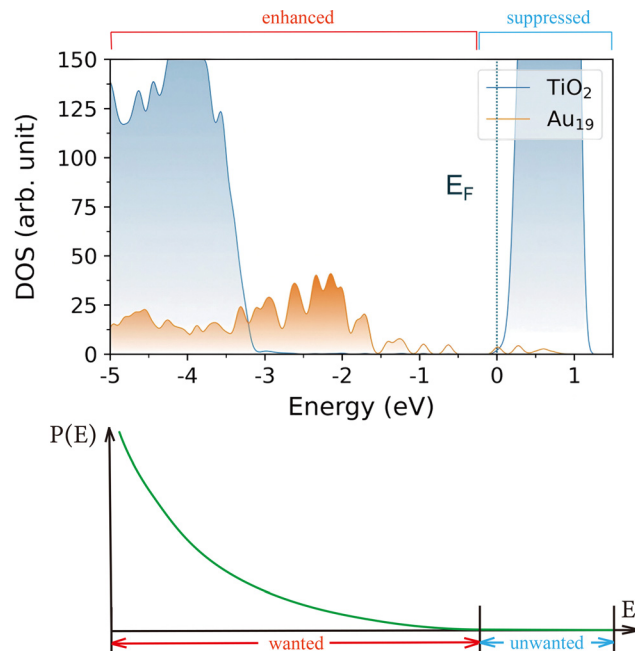


Fig. 4 Illustration of the ideal polynomial that enhances the wanted spectrum region and suppresses the unwanted spectrum region.

new wavefunctions:

$$\Psi' \xrightarrow{\text{orthonormalization}} \Phi \quad (16)$$

Gram-Schmit procedure⁵³ is common for orthonormalization, but Cholesky QR⁵⁴ can be a more efficient alternative.

2.4.3 Rayleigh-Ritz step. Afterwards, we can then project the real Hamiltonian into the filtered, orthonormal subspace, solve the subspace eigenvalue problem, and project the wavefunction back through the standard Rayleigh-Ritz steps.⁵⁵

Suppose that the original full space wavefunction Ψ and the projected subspace wavefunction Φ are linked by a transformation matrix Q . Then the KS equations are satisfied as such:

$$H\Psi = E\Psi \Leftrightarrow H(\Phi Q) = E(\Phi Q) = (\Phi Q)E \quad (17)$$

where E is a diagonal matrix containing non-increasingly ordered eigenvalues of H . Left-projected by Φ^\dagger , and use the orthonormality of Φ , we have:

$$(\Phi^\dagger H \Phi)Q = (\Phi^\dagger \Phi)QE = QE \quad (18)$$

We note $\hat{H} = \Phi^\dagger H \Phi$ as the projected Hamiltonian. After solving this projected eigenvalue problem, we can get the transformation matrix Q to obtain the original full space wavefunction Ψ :

$$\hat{H} = \Phi^\dagger H \Phi \rightarrow \hat{H}Q = QE \rightarrow \Psi = \Phi Q \quad (19)$$

2.4.4 Space-filling curves. As discussed above, the dimension of the Hamiltonian matrix in the real-space representation is extremely large. However, it is quite sparse because of the close-to-diagonal kinetic component and the short-range character of the nonlocal potential component. Therefore, it is not wise to do the normal matrix-vector multiplication using the

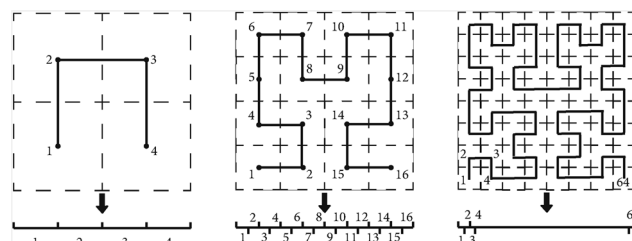


Fig. 5 Examples of Hilbert SFCs that map the two-dimensional grids into a one-dimensional curve and preserve the locality and self-similarity.

entire matrix, especially when we need to solve the KS equation iteratively. For better use of computational resources rather than computation of many zeros, an efficient and parallelizable sparse matrix-vector (SpMV) multiplication algorithm is essential. Leveraging space filling curves (SFCs) to partition the computational domain is an effective approach to minimize communication overhead and improve parallel performance.^{56–59}

SFCs are mathematical constructs that map multi-dimensional space onto a one-dimensional path while preserving locality and self-similarity.^{60,61} Traditional Cartesian partitioning often leads to poor load balancing and excessive inter-processor communication. SFC-based partitioning solves this by reordering grid points into a structured sequence, improving memory access, and reducing data transfer costs.^{62,63} Among various SFCs, the Hilbert curve stands out due to its superior locality preservation.⁶⁰ The locality preservation means that grids that are spatially close will remain adjacent along the SFC. This minimizes communication between processors, improving efficiency. Additionally, Hilbert SFCs coupled with blockwise operations enhance vector processing capabilities by grouping multiple grid points, and further optimizing computational performance.^{64,65} Fig. 5 illustrates the two-dimensional versions of the Hilbert SFCs that convert all grids into one dimension.

With the help of Hilbert SFCs, the computations are remarkably accelerated. Compared to the normal Cartesian partition, blockwise Hilbert SFCs achieved a 6-time speedup and the scalability went up to 512 processors, whereas traditional methods struggle beyond 100 processors.³⁰ These improvements enabled PARSEC's simulation of silicon nanocrystals with over 26 000 atoms, while accurately capturing Van Hove singularities in the density of states.³⁰ These results demonstrate the importance of Hilbert SFCs in large-scale real-space electronic structure calculations and suggest their potential application in other computational fields requiring efficient grid partitioning.

2.5 Predicting experimental XPS CEBE through PPs development

Within the PP framework, our group developed a method to predict the XPS CEBE,²⁴ which connects the real-space FDPP method with real observables in experiments.

XPS CEBE (E_b) is defined as:

$$E_b = E^{N-1}[n_F] - E^N[n_I] \quad (20)$$

where $E^{N-1}[n_F]$ and $E^N[n_I]$ are the energy functionals of the final core excited state and the initial ground state, respectively, and n represents the AE density. In our previous work,²⁴ an estimation was derived based on the accuracy of cohesive energies obtained by PPs:

$$E[n] \approx E[\rho] - \sum_a^{N_a} E[\rho_a] + \sum_a^{N_a} E[n_a] \quad (21)$$

where N_a is the number of atoms in the system, ρ represents the PP density, and $E[\rho_a]$, $E[n_a]$ denote the AE, PP energy functionals of the a -th isolated atom, which can be conveniently obtained from the PP generator.⁶⁶ With eqn (20) and (21), the CEBEs of non-metal elements in the 2nd row²⁴ (B, C, N, O) and the 3rd row²⁶ (P, S) were investigated within the Δ SCF^{25,67–75} scheme using the real-space PP method implemented in ARES.¹² The PP results are consistent with the AE results simulated from Qchem² using MOM⁷⁶ or SGM,⁷⁷ and are comparable with the experimental results. The mean absolute errors (MAE) of the AE and PP CEBE shifts for those elements with respect to the experiments are summarized in Table 2.

In addition, the results from two different boundary conditions, the periodic boundary condition (PBC) and DBC, are compared. To converge the energy of the charged system, PBC requires a much larger supercell size than DBC due to its unavoidable inclusion of strong electrostatic interactions between supercells.²⁴ However, if the electron holes are not delocalized,⁷⁸ one can use the Makov–Payne equation⁷⁹ to correct the core–hole interactions⁷⁵ by setting a sufficiently large supercell.²⁶ To test the applicability of the real-space KS-DFT PP method for large-scale systems, the O-1s CEBE shifts in protonated water clusters $[H_3O^+ \cdots (H_2O)_n, n \leq 20]$,²⁴ and the Si-2p CEBE shifts of HZSM5 as well as its deprotonated counterparts²⁶ with respect to ZSM5^{80–82} were also investigated.

3 Applications

3.1 Characterizing air–water interactions in nanodroplets with real-space KS-DFT

Understanding ion behavior at the air–water interfaces is crucial for diverse chemical and environmental processes,

Table 2 Mean absolute errors of 1s, 2s, and 2p_{3/2} CEBE Shifts of B, C, N, O, S and P in molecules with respect to the experiments (in eV)^{24,26}

Core	Element	AE		PP	
		PBE	SCAN	B3LYP	PBE
1s	B	0.27		0.06	0.23
	C	0.38		0.12	0.20
	N	0.14		0.12	0.15
	O	0.11		0.10	0.11
	S	0.65	0.22		0.70
	P	0.30	0.09		0.32
2s	S	0.38	0.26		0.40
	P	0.24	0.49		0.22
2p _{3/2}	S	0.32	0.16		0.33
	P	0.25	0.13		0.31



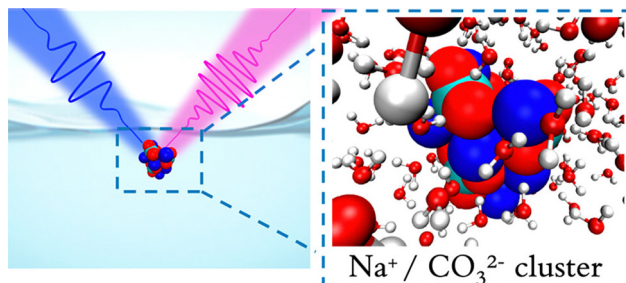


Fig. 6 Schematic of the experimental design for probing a carbonate cluster residing near the liquid water surface. Figure is reproduced with permission from ref. 88, Copyright 2023 American Chemical Society and licensed under a Creative Commons License CC BY 4.0, respectively.

with potential impacts ranging from atmospheric aerosol chemistry,^{83–85} uptake of gases at the ocean surface,⁸⁶ and myriad biological processes. Here, we showcase our work of CO₂ dissolution in the NaCl nanodroplets (see Fig. 6). Insights gained from this study can be applied to ocean acidification and mammalian respiration physiology. Classical electrostatic theory⁸⁷ predicts that doubly charged carbonate ions (CO₃²⁻) should have much higher solvation energies than singly charged bicarbonate ions (HCO₃⁻). As a result, carbonate ions are expected to reside predominantly in the bulk, where they can be fully solvated, while bicarbonate ions, with their lower charge and solvation energy, are more likely to populate the interface. However, recent experimental work by Devlin *et al.*⁸⁸ employing resonantly enhanced deep-UV second-harmonic generation (DUV-SHG) spectroscopy revealed counterintuitive behaviors at these interfaces, such as the enhanced concentration of carbonate anions over bicarbonate anions at the air–water interface, contradicting the classical electrostatic expectations. This unexpected surface affinity demands additional characterization validation and mechanistic insights beyond conventional atomistic models.

Simulating such complex interfaces poses significant challenges for traditional DFT methods due to the sheer number of atoms (on the order of thousands) required in the simulation box to capture local variances and long-range phenomena. Real-space KS-DFT addresses these challenges by providing a framework that naturally handles nonperiodicity, disorder, and efficient parallelization of large-scale simulations, making it uniquely suited for exploring heterogeneous environments like nanodroplets. Furthermore, the recent development of surface-sensitive XPS prediction capabilities within the real-space KS-DFT framework^{24,26} offers a new avenue for directly linking computational results to experimental observables.

Accelerated molecular dynamics (MD) simulations were initially performed by Jamnuch *et al.*,⁸⁸ which were used to generate snapshots for the electronic structure calculations. Each set of simulations had representative structures of the targeted carbon containing chemical species at the air–water interface and in the bulk. Then, we calculated the C 1s CEBEs for carbonate and bicarbonate at the air–water interface using real-space KS-DFT code ARES. Due to the enormous

computational cost associated, a novel PBE(B3LYP) one-shot strategy was developed in ARES to further accelerate these calculations while maintaining a desired accuracy that is comparable to AE-B3LYP.²⁴ This entails non-SCF calculations at the B3LYP level based on the converged PBE charge density. As a result, all calculations reported were performed at this PBE(B3LYP) level. As shown in Fig. 7(a), our calculations reveal that the XPS spectra were invariant to the displacement of the anion relative to the air–water interface as well as to the coordination number of the carbonate species. In Fig. 7(b), the surface-sensitive AP-XPS spectra measured by Lam *et al.*⁸⁹ are reproduced. The relative shift between the experimental carbonate/bicarbonate spectral signatures agrees well with the shift in the calculated binding energies, with a difference of only 0.1 eV, indicating indeed that the spectral fitting and relative concentrations reported by Lam *et al.*⁸⁹ are of the distinct carbonate/bicarbonate peaks and not some convolution of the two due to spectral shifts. By tuning the incident photon energy, the experiments can explore different attenuation lengths of the emitted photoelectron with a depth profiling as shallow as ~2 nm, therefore gaining interfacial concentration information for the different ions presented in the system. Finally, these calculations support the hypothesis that strong ion pairing of CO₃²⁻ with Na⁺ counterions leads to the formation of near neutral agglomerates,

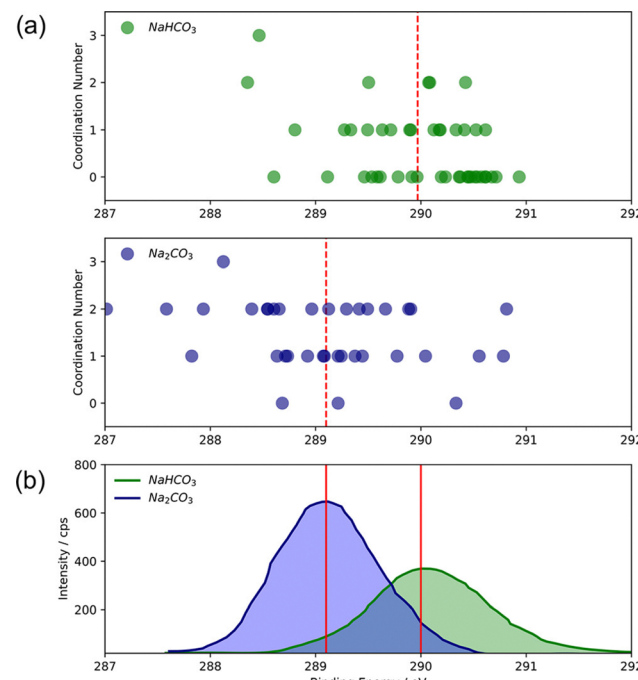


Fig. 7 (a) Simulated XPS CEBEs for C(1s) excitation of carbonate and bicarbonate at the air–water interface. Individual data points indicate the calculated CEBE and the associated coordination number with the anion. Calculated binding energies are “energy-aligned” to the experimental carbonate peak at 289.1 eV. (b) C(1s) XPS binding energies with an incident photon energy of 490 eV from 0.5 M solutions of NaHCO₃ and Na₂CO₃ and their CEBE shift estimated from the real-space PP methods. Reproduced with permission from ref. 88, Copyright 2023 American Chemical Society and licensed under a Creative Commons License CC BY 4.0, respectively.



which are more surface affinity than their singly charged bicarbonate counterparts.

3.2 Studying carbon capture near the DAC limit with real-space KS-DFT

The rising concentration of atmospheric CO_2 has intensified the search for effective carbon capture strategies,^{90–92} with DAC emerging as an intriguing avenue due to its potential for negative emissions. However, capturing CO_2 directly from air presents unique challenges, stemming from its low concentration (~ 400 ppm) and the weak adsorption characteristics of CO_2 , a linear molecule with high kinetic stability. Consequently, DAC systems require adsorbents capable of both effective CO_2 capture under these dilute conditions and efficient release during regeneration to minimize energy costs.⁹³

Our vision, as shown in Fig. 8, is to couple carbon-based solid sorbents with a steam-assisted temperature vacuum swing desorption (TVSD) process for energy- and cost-effective carbon capture and release. Activated carbon (AC)-based sorbents, derived from abundant and economical resources like wood and biochar, offer a promising pathway for scalable DAC. These materials can be chemically and structurally engineered to preferentially adsorb CO_2 over other atmospheric gases like N_2 and O_2 , while high-temperature steam aids desorption by driving CO_2 into a collection reservoir. Integrating these materials into a dynamic energy supply has the potential to further reduce the overall cost of carbon capture. To identify optimal AC-based adsorbents for DAC applications, Glenna *et al.*⁹⁴ proposed a hierarchical selection criterion integrating experimental insights and computational techniques. The primary criterion focuses on the CO_2 adsorption energy, E_{ads} , which determines the balance between strong binding for effective capture and weak binding for energy-efficient desorption. E_{ads} is defined as:

$$E_{\text{ads}} = E_{\text{Graphene}_{\text{der}} + \text{CO}_2} - (E_{\text{Graphene}_{\text{der}}} + E_{\text{CO}_2}) \quad (22)$$

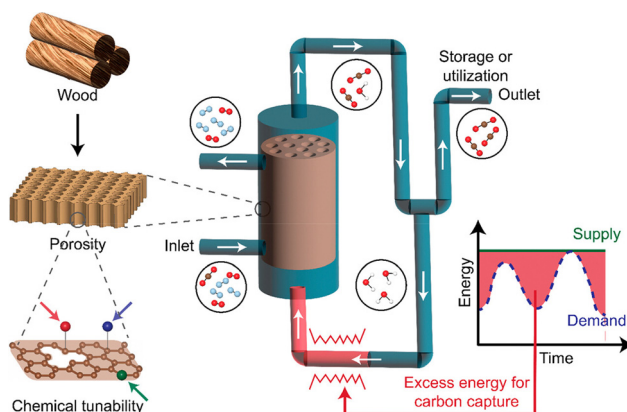


Fig. 8 Schematic showing the steam-assisted temperature vacuum swing desorption process with wood-derived AC as the CO_2 adsorbent. Graphene-derived materials are suitable templates for evaluating AC-based materials. Integrating with a dynamic energy supply results in energy- and cost-effective solutions for carbon capture. Figure is reproduced with permission from ref. 94 under a Creative Commons License CC BY 4.0.

where all terms represent the total energies of the respective relaxed structures. An optimal E_{ads} of -0.41 eV was identified, marking the boundary between physical and chemical adsorption. Various dopants, functional groups, and structural modifications were examined *via* DFT simulations to tune E_{ads} to this ideal value. Notably, methylamine (NH_2CH_3) and pyridine ($\text{C}_5\text{H}_5\text{N}$) decorated graphene achieved this balance through an insertion mechanism.⁹⁵ Secondary criteria ensured long-term feasibility by considering thermal stability, defect sensitivity, and gas selectivity. Thermal stability is critical for maintaining structural integrity during high-temperature desorption cycles, ensuring consistent performance over time. Defect sensitivity accounts for real-world material imperfections that may affect adsorption properties. Selectivity of CO_2 over other gases like N_2 and O_2 is equally important for practical deployment. Finally, ternary criteria focused on mimicking adsorption capacity under realistic environmental conditions by incorporating both selectivity and surface coverage into the evaluation.

A critical question that arose from this framework was whether E_{ads} changes when system size increases to reflect the near-zero surface coverage relevant to DAC conditions. Traditional DFT methods, constrained by scaling limitations, cannot easily probe these effects, making it difficult to assess adsorption behavior at ultra-low coverages. Real-space KS-DFT, however, addresses this gap by enabling simulations at the scale required to explore such regimes, leveraging favorable parallelization.

To study coverage effects, the Langmuir isotherm model was applied to predict CO_2 coverage on graphene:

$$\theta = \frac{kp}{1 + kp} \quad (23)$$

where θ is the coverage (CO_2 molecules per carbon atom), k is the Langmuir constant (1.12 bar^{-1} for CO_2), and p is the partial pressure of the gas (bar). At 400 ppm, the pristine graphene (PG) surface coverage for CO_2 is around 2211 carbon atoms per CO_2 molecule. Simulating such large systems is infeasible for

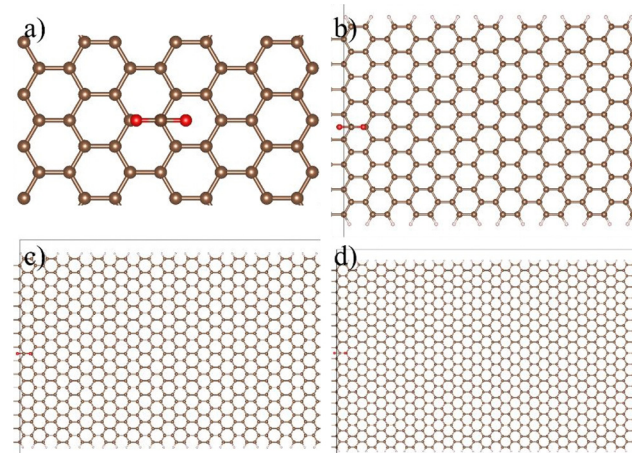


Fig. 9 Single point configuration of CO_2 on PG in 36 (a), 252 (b), 780 (c), and 1152 (d) C atom sheets using ARES. Figure is reproduced with permission from ref. 94 under a Creative Commons License CC BY 4.0.



Table 3 $\text{CO}_2 E_{\text{ads}}$ (eV) on PG with respect to coverage

CO_2 concentration (ppm)	25 000	3520	1135	768
# C atoms/ CO_2 molecule	36	252	780	1152
PG (ARES)	−0.201	−0.194	−0.196	−0.192

conventional plane-wave-based DFT methods, making real-space KS-DFT essential for capturing these low-coverage effects.

Using ARES, real-space KS-DFT calculations were performed to predict CO_2 adsorption on PG sheets containing 36, 252, 780, and 1152 carbon atoms (Fig. 9). Importantly, the result for the 36-carbon atom system was validated against an exemplary Quantum Espresso calculation at the same level of theory, confirming the accuracy of the real-space KS-DFT approach. Results showed that E_{ads} converges rapidly even with relatively small simulation boxes, as shown in Table 3. Importantly, the adsorption energy remained consistent across different system sizes, indicating that enthalpy alone does not significantly affect coverage. As such, conventional DFT methods are likely sufficient to accurately capture thermodynamic properties like E_{ads} for AC-based DAC materials.

4 Alternative methods for large-scale simulations

In addition to the real-space DFT techniques, recent years witnessed exciting booming in other method developments for large-scale simulations.

Orbital-free DFT (OF-DFT) bypasses the need to compute Kohn–Sham orbitals and instead approximates the total energy directly as a functional of the electron density. This enables formally linear scaling with system size, making OF-DFT attractive for large-scale simulations.^{96–101} However, a key limitation of OF-DFT lies in the construction of accurate orbital-free kinetic energy functionals (KEFs).^{96,102} Additionally, by design, OF-DFT does not yield wavefunctions, and as such, it cannot be directly used to compute spectroscopic properties. Machine learning (ML) approach¹⁰³ can be useful, but usually with a total energy focus and at high cost in terms of physics and explainability. Therefore, while OF-DFT and ML approaches represent powerful additions to the computational toolbox for large-scale materials simulations, they often complement rather than replace the capabilities of real-space KS-DFT, especially in scenarios where electronic structure solution and spectroscopic accuracy are critical, such as in the example of nanodroplet. In this case, the absence of explicit wavefunctions in OF-DFT makes it unsuitable for spectroscopic simulations such as XPS, where access to orbital information is essential for accurately predicting CEBE. By contrast, real-space KS-DFT provides direct access to the electronic structure, enabling reliable and accurate spectroscopic predictions in such complex, inhomogeneous environments. Moreover, for systems like graphene with delocalized character, the construction of accurate KEFs becomes particularly problematic, while real-space DFT overcomes this limitation.

Likewise, other linear-scaling DFT frameworks have been developed to reduce the computational complexity of electronic

structure simulations by avoiding explicit diagonalization of the Kohn–Sham Hamiltonian. These methods rely on the locality of the electronic density matrix and typically reformulate DFT in terms of localized orbitals or sparse density matrices by truncation, enabling formal linear scaling with system size. Examples include ONETEP, which uses variationally optimized non-orthogonal generalized Wannier functions (NGWFs),^{104,105} CONQUEST, which employs localized support functions with density matrix minimization,^{106,107} and BigDFT, which leverages wavelet bases to capture real-space locality efficiently.^{108,109} While these methods are powerful for modeling large insulating and semiconducting systems, it remains challenging to construct a single and generalizable scheme that yields accurate and transferable descriptions of metals, molecules, and heterogeneous systems. In particular, linear-scaling DFT techniques often require strict localization of orbitals or density matrices, which breaks down for delocalized states or systems with long-range interactions. As such, while linear-scaling DFT methods complement conventional and real-space KS-DFT in certain regimes, they do not fully replace them, particularly in charged, metallic, or highly delocalized systems, like the absorption of CO_2 on graphene. For graphene, the delocalized π -electron structure poses a significant challenge to linear-scaling DFT approaches, which depend on strict localization of orbitals or density matrices. In contrast, real-space KS-DFT handles both localized adsorption interactions and extended delocalized states without imposing localization constraints, making it better suited for such systems. Likewise, the nanodroplet involves long-range ion–ion interactions, which violate the locality assumptions required for density matrix truncation or localized orbitals, whereas real-space KS-DFT can capture both short- and long-range interactions without enforcing localization.

5 Outlook

As energy applications grow increasingly complex, the need for computational tools capable of accurately simulating large, disordered systems with unbalanced charge is becoming more evident. Real-space KS-DFT has shown promise in addressing these challenges, as demonstrated by its application to the air–water interface in nanodroplets and carbon capture near the DAC limit. In both cases, real-space KS-DFT enabled simulations of large, non-periodic systems and captured subtle interfacial effects that conventional DFT methods and other linear-scaling techniques could yet resolve. These examples highlight the method's ability to provide valuable insights into complex chemical environments at scales relevant to practical applications. As research continues to tackle more intricate problems in energy storage, conversion, and environmental remediation, real-space KS-DFT is poised to become an increasingly important tool for computational chemistry and materials science.

From a computational perspective, the transition into the exascale era presents new opportunities for leveraging HPC infrastructure. For example, Oak Ridge National Laboratory's Frontier supercomputer¹¹⁰ – the first to break the exascale barrier – performs over a quintillion calculations per second,



enabling simulations at unprecedented scales. Real-space KS-DFT's inherently parallelizable structure aligns well with large-scale HPC environments, making it particularly suited for heterogeneous CPU-GPU architectures. As computational power grows, improving the efficiency of distributed algorithms – particularly for operations and memory management – will be crucial to realizing the full potential of this method. The increasing complexity of modern simulations calls for the continued adoption and development of real-space KS-DFT to address scientific challenges that demand large-scale modeling.

Recently, the real-space DFT community has made notable progress, and various codes now support a broad range of applications. For instance, OCTOPUS enables real-time and linear-response time-dependent DFT (TDDFT) calculations,¹¹¹ making it well suited for computing optical absorption spectra, dielectric functions, and photoelectron spectra.¹¹² DFT-FE and SPARC now support CPU-GPU heterogeneous architectures,^{19,113} further advancing real-space DFT toward the exascale era. PARSEC has also implemented more efficient subspace filtering techniques and eigenvalue solvers, enhancing its computational performance.^{114–116} In addition, PARSEC provides real-space implementations for systems with general or partial periodicity by directly incorporating Bloch's theorem into the Kohn–Sham equations.¹¹⁷ Combined with appropriate *k*-point sampling techniques, this enables calculations of band structures and densities of states (DOS).

Despite its strengths, real-space DFT also faces key challenges that currently limit its broader adoption. One major issue is that, compared to traditional basis-based methods, it is much more memory-intensive, especially when using fine grids. A powerful strategy to address this is the use of matrix-free methods, where the Hamiltonian is never stored explicitly but applied on-the-fly during matrix-vector multiplications. The Laplacian-vector products can be computed directly using FD stencils or FE operators.¹¹⁸ This drastically reduces memory usage and enables highly scalable matrix-vector operations. Similar strategies can be used to handle the nonlocal part of the Hamiltonian as well. Moreover, adaptive mesh refinement (AMR)^{50,51} can be employed to concentrate grid resolution near nuclei or chemical interfaces while using coarser grids elsewhere, reducing the number of required grid points for systems with high spatial heterogeneity. Another major issue is the computational cost of diagonalizing the sparse Hamiltonians. Even though advanced techniques such as Chebyshev subspace filtering and Rayleigh–Ritz projection are under active development to reduce this bottleneck by focusing only on the eigenspace near occupied levels, further algorithmic implementations for sparse-matrix eigensolvers^{119,120} or alternative strategies towards linear-scaling are worth exploring. One possible idea is to gain inspiration from density matrix purification^{121,122} that avoids the direct diagonalization of the Hamiltonian. Additionally, the Hartree potential evaluation step is often time-consuming for large systems. Therefore, efficient Poisson solvers^{123–125} for both periodic and non-periodic systems are critical for accelerating the simulations.

In terms of *status quo*, certain capabilities remain more mature in conventional plane-wave and localized basis set codes. For example, hybrid functional calculations involving exact exchange are not yet fully implemented in real-space DFT frameworks due to the significant computational cost associated with the nonlocal nature of Fock exchange. However, strategies such as projection schemes have been proposed,^{126,127} and the ARES team has implemented a one-shot B3LYP (double hybrid functional) strategy based on the wavefunctions from PBE calculations.^{24,26} The SPARC team also has made notable progress in this area recently.¹²⁸ Features such as phonon calculations, density functional perturbation theory (DFPT) or double hybrid, and response properties like Raman and dielectric tensors are also less commonly implemented in real-space frameworks compared to well-established packages like VASP or Quantum Espresso. Furthermore, real-space codes often rely on norm-conserving PPs and may lack support for PAW, ultrasoft PPs or relativistic effects, which are important for transition metals and heavy elements. Finally, compared to mainstream DFT codes, real-space codes currently offer limited support for high-throughput workflows, automated job management, and integration with materials databases. A more mature ecosystem will be essential for accelerating discovery and enabling complex, multi-step simulations, particularly in large-scale screening and materials design efforts. Bridging this gap will be important for broadening the adoption of real-space methods and ensuring their accessibility to a wider research community.

Looking ahead, further methodological developments are needed to keep pace with the hardware advancements.^{129,130} Establishing new protocols for modularization and interoperability will help real-space KS-DFT integrate more seamlessly into broader computational frameworks. Additionally, advancements in exchange–correlation functionals,³⁸ post-DFT methods,^{19,107,109} excited-state techniques,^{131,132} and fast molecular dynamics^{133,134} will remain essential to enhancing predictive accuracy and expanding the method's applicability. Importantly, as real-space KS-DFT matures, identifying unique applications where its massive parallelization capabilities are truly warranted will help ensure its continued impact in both method development and scientific discovery. The path forward lies not only in scaling computations but also in finding the right questions to answer with this powerful approach.

Conclusions

Real space KS-DFT has emerged as a compelling computational framework capable of meeting the increasing demands of modern electronic structure problems. This article reviewed the foundational theories, algorithmic developments, and recent applications that illustrate the method's potential for tackling large, complex, and disordered systems. Through a FDPP approach, real-space KS-DFT enables scalable, accurate simulations of complicated systems while naturally integrating with HPC architectures. We demonstrated the predictive power of real-space KS-DFT in chemically and environmentally



relevant systems. From capturing the nuanced behavior of carbonates at air–water interfaces to modeling CO₂ adsorption in carbon-based sorbents under DAC conditions, the method proves effective in bridging quantum-scale phenomena with experimental observables. Notably, innovations such as real-space XPS predictions and efficient algorithmic strategies (e.g., subspace filtering and space-filling curve partitioning) further enhance the method's capability and performance. Looking forward, as computational chemistry continues to scale into the exascale era, real-space KS-DFT is poised to play an important role through its parallelization capability. Continued progress in methodological development, especially in exchange–correlation approximations, excited-state modeling, and real-time dynamics, will be essential to fully realize its impact. Ultimately, real-space KS-DFT represents not just a technical advancement, but a versatile toolset for exploring the frontiers of chemical and materials discovery.

Author contributions

J. Q. acquired funding for, and led the project. Z. Z. and J. Q. conceptualized the project and wrote the first manuscript. All authors contributed to reviewing and editing the manuscript under the supervision of J. Q.

Code availability

The ARES code cited in the paper is currently proprietary. The first real-space code PARSEC from James R. Chelikowsky's group is available on Github: <https://github.com/PARSEC-real-space-code/PARSEC>. The Matlab version of PARSEC is also available on Github: https://github.com/PARSEC-real-space-code/Matlab_Real_Space.

Data availability

The data mentioned in this article can be found in corresponding references. There are no extra data associated with this article.

Conflicts of interest

There are no conflicts to declare.

Acknowledgements

This work is supported by the Early Career Research Award Program from the U.S. Department of Energy, Office of Science, Office of Basic Energy Sciences, Chemical Sciences, Geosciences and Biosciences Division, through Contract No. DE-AC02-05CH11231.

References

- 1 N. Marzari, A. Ferretti and C. Wolverton, *Nat. Mater.*, 2021, **20**, 736–749.
- 2 E. Epifanovsky, A. T. Gilbert, X. Feng, J. Lee, Y. Mao, N. Mardirossian, P. Pokhilko, A. F. White, M. P. Coons and A. L. Dempwolff, *J. Chem. Phys.*, 2021, **155**, 084801.
- 3 M. J. Frisch, G. W. Trucks, H. B. Schlegel, G. E. Scuseria, M. A. Robb, J. R. Cheeseman, G. Scalmani, V. Barone, G. A. Petersson, H. Nakatsuji *et al.* *Gaussian~16 Revision C.01*, Gaussian Inc., Wallingford CT, 2016.
- 4 G. Kresse and J. Furthmüller, *Phys. Rev. B:Condens. Matter Mater. Phys.*, 1996, **54**, 11169.
- 5 G. Kresse and J. Furthmüller, *Comput. Mater. Sci.*, 1996, **6**, 15–50.
- 6 P. Giannozzi, S. Baroni, N. Bonini, M. Calandra, R. Car, C. Cavazzoni, D. Ceresoli, G. L. Chiarotti, M. Cococcioni and I. Dabo, *et al.*, *J. Phys.: Condens. Matter*, 2009, **21**, 395502.
- 7 J. R. Chelikowsky, N. Troullier and Y. Saad, *Phys. Rev. Lett.*, 1994, **72**, 1240.
- 8 J. R. Chelikowsky, N. Troullier, K. Wu and Y. Saad, *Phys. Rev. B:Condens. Matter Mater. Phys.*, 1994, **50**, 11355.
- 9 L. Kronik, A. Makmal, M. L. Tiago, M. Alemany, M. Jain, X. Huang, Y. Saad and J. R. Chelikowsky, *Phys. Status Solidi B*, 2006, **243**, 1063–1079.
- 10 M. Dogan, K.-H. Liou and J. R. Chelikowsky, *J. Chem. Phys.*, 2023, **158**, 244114.
- 11 M. Segall, P. J. Lindan, M. A. Probert, C. J. Pickard, P. J. Hasnip, S. Clark and M. Payne, *J. Phys.: Condens. Matter*, 2002, **14**, 2717.
- 12 Q. Xu, S. Wang, L. Xue, X. Shao, P. Gao, J. Lv, Y. Wang and Y. Ma, *J. Phys.: Condens. Matter*, 2019, **31**, 455901.
- 13 V. Michaud-Rioux, L. Zhang and H. Guo, *J. Comput. Phys.*, 2016, **307**, 593–613.
- 14 M. A. Marques, A. Castro, G. F. Bertsch and A. Rubio, *Comput. Phys. Commun.*, 2003, **151**, 60–78.
- 15 X. Andrade, D. Strubbe, U. De Giovannini, A. H. Larsen, M. J. Oliveira, J. Alberdi-Rodriguez, A. Varas, I. Theophilou, N. Helbig and M. J. Verstraete, *et al.*, *Phys. Chem. Chem. Phys.*, 2015, **17**, 31371–31396.
- 16 Q. Xu, A. Sharma, B. Comer, H. Huang, E. Chow, A. J. Medford, J. E. Pask and P. Suryanarayana, *SoftwareX*, 2021, **15**, 100709.
- 17 B. Zhang, X. Jing, Q. Xu, S. Kumar, A. Sharma, L. Erlandson, S. J. Sahoo, E. Chow, A. J. Medford and J. E. Pask, *et al.*, *Software Impacts*, 2024, **20**, 100649.
- 18 P. Motamarri, S. Das, S. Rudraraju, K. Ghosh, D. Davydov and V. Gavini, *Comput. Phys. Commun.*, 2020, **246**, 106853.
- 19 S. Das, P. Motamarri, V. Subramanian, D. M. Rogers and V. Gavini, *Comput. Phys. Commun.*, 2022, **280**, 108473.
- 20 M. Lopez del Puerto, M. L. Tiago, I. Vasiliev and J. R. Chelikowsky, *Phys. Rev. A:At., Mol., Opt. Phys.*, 2005, **72**, 052504.
- 21 S. J. Sahoo, X. Jing, P. Suryanarayana and A. J. Medford, *J. Phys. Chem. C*, 2022, **126**, 2121–2130.
- 22 S. J. Sahoo, Q. Xu, X. Lei, D. Staros, G. R. Iyer, B. Rubenstein, P. Suryanarayana and A. J. Medford, *ChemPhysChem*, 2024, **25**, e202300688.
- 23 J. Qian, A. Baskin, Z. Liu, D. Prendergast and E. J. Crumlin, *J. Chem. Phys.*, 2020, **153**, 044709.
- 24 Q. Xu, D. Prendergast and J. Qian, *J. Chem. Theory Comput.*, 2022, **18**, 5471–5478.
- 25 J. Qian, E. J. Crumlin and D. Prendergast, *Phys. Chem. Chem. Phys.*, 2022, **24**, 2243–2250.
- 26 L. Liu, Q. Xu, L. dos Anjos Cunha, H. Xin, M. Head-Gordon and J. Qian, *J. Chem. Theory Comput.*, 2024, **20**, 6134–6143.
- 27 Y. Zhou, Y. Saad, M. L. Tiago and J. R. Chelikowsky, *J. Comput. Phys.*, 2006, **219**, 172–184.
- 28 Y. Zhou, Y. Saad, M. L. Tiago and J. R. Chelikowsky, *Phys. Rev. E:Stat., Nonlinear, Soft Matter Phys.*, 2006, **74**, 066704.
- 29 J. MacDonald, *Phys. Rev.*, 1933, **43**, 830.
- 30 K.-H. Liou, A. Biller, L. Kronik and J. R. Chelikowsky, *J. Chem. Theory Comput.*, 2021, **17**, 4039–4048.
- 31 P. Hohenberg and W. Kohn, *Phys. Rev.*, 1964, **136**, B864.
- 32 W. Kohn and L. J. Sham, *Phys. Rev.*, 1965, **140**, A1133.
- 33 J. P. Perdew, K. Burke and M. Ernzerhof, *Phys. Rev. Lett.*, 1996, **77**, 3865.
- 34 S. Kümmel and J. P. Perdew, *Phys. Rev. B:Condens. Matter Mater. Phys.*, 2003, **68**, 035103.
- 35 V. I. Anisimov, F. Aryasetiawan and A. Lichtenstein, *J. Phys.: Condens. Matter*, 1997, **9**, 767.
- 36 M. Cococcioni and S. De Gironcoli, *Phys. Rev. B:Condens. Matter Mater. Phys.*, 2005, **71**, 035105.



37 H. J. Kulik, M. Cococcioni, D. A. Scherlis and N. Marzari, *Phys. Rev. Lett.*, 2006, **97**, 103001.

38 N. Mardirossian and M. Head-Gordon, *Mol. Phys.*, 2017, **115**, 2315–2372.

39 R. M. Martin, *Electronic structure: basic theory and practical methods*, Cambridge University Press, Cambridge, 2nd edn, 2020.

40 H. Hellmann, *J. Chem. Phys.*, 1935, **3**, 61.

41 J. C. Phillips and L. Kleinman, *Phys. Rev.*, 1959, **116**, 287.

42 M. H. Cohen and V. Heine, *Phys. Rev.*, 1961, **122**, 1821.

43 D. Hamann, M. Schlüter and C. Chiang, *Phys. Rev. Lett.*, 1979, **43**, 1494.

44 N. Troullier and J. L. Martins, *Phys. Rev. B: Condens. Matter Mater. Phys.*, 1991, **43**, 1993.

45 D. Vanderbilt, *Phys. Rev. B: Condens. Matter Mater. Phys.*, 1990, **41**, 7892.

46 G. Kresse and D. Joubert, *Phys. Rev. B: Condens. Matter Mater. Phys.*, 1999, **59**, 1758.

47 G. Kerker, *J. Phys. C*, 1980, **13**, L189.

48 L. Kleinman and D. Bylander, *Phys. Rev. Lett.*, 1982, **48**, 1425.

49 B. Fornberg, *SIAM Rev.*, 1998, **40**, 685–691.

50 M. J. Berger and P. Colella, *J. Comput. Phys.*, 1989, **82**, 64–84.

51 M. J. Berger and J. Oliger, *J. Comput. Phys.*, 1984, **53**, 484–512.

52 C. Lanczos, *J. Res. Natl. Bur. Stand.*, 1950, **45**, 255–282.

53 W. Cheney and D. Kincaid, *Aust. Math. Soc.*, 2009, **110**, 544–550.

54 C. Benoit, *Bull. Geod.*, 1924, **2**, 67–77.

55 L. N. Trefethen and D. Bau, *Numerical linear algebra*, SIAM, Philadelphia, 25th Anniversary edn, 2022.

56 H. Sagan, *Space-filling curves*, Springer Science & Business Media, New York, 2012.

57 J. K. Lawder and P. J. King, British National Conference on Databases, 2000, pp. 20–35.

58 P. Xu and S. Tirthapura, *ACM Trans. Database Syst.*, 2014, **39**, 1–27.

59 A.-J. N. Yzelman and D. Roose, *IEEE Trans. Parallel Distrib. Syst.*, 2013, **25**, 116–125.

60 B. Moon, H. V. Jagadish, C. Faloutsos and J. H. Saltz, *IEEE Trans. Knowl. Data Eng.*, 2001, **13**, 124–141.

61 S. P. Sastry, E. Kultursay, S. M. Shontz and M. T. Kandemir, *Eng. Comput.*, 2014, **30**, 535–547.

62 R. Borrell, J. C. Cajas, D. Mira, A. Taha, S. Koric, M. Vázquez and G. Houzeaux, *Comput. Fluids*, 2018, **173**, 264–272.

63 S. Schamberger and J.-M. Wierum, *Future Gener. Comput. Syst.*, 2005, **21**, 759–766.

64 K. P. Lorton and D. S. Wise, *ACM SIGARCH Comput. Archit. News*, 2007, **35**, 6–12.

65 C. Yount, J. Tobin, A. Breuer and A. Duran, 2016 Sixth International Workshop on Domain-Specific Languages and High-Level Frameworks for High Performance Computing (WOLFHPC), 2016, pp. 30–39.

66 M. Fuchs and M. Scheffler, *Comput. Phys. Commun.*, 1999, **119**, 67–98.

67 P. S. Bagus, *Phys. Rev.*, 1965, **139**, A619.

68 J. Q. Broughton and D. L. Perry, *J. Chem. Soc., Faraday Trans. 2*, 1977, **73**, 1320–1327.

69 P. Bagus and M. Seel, *Phys. Rev. B: Condens. Matter Mater. Phys.*, 1981, **23**, 2065.

70 P. Bagus, A. Rossi and P. Avouris, *Phys. Rev. B: Condens. Matter Mater. Phys.*, 1985, **31**, 1722.

71 C. Flynn and N. Lipari, *Phys. Rev. B*, 1973, **7**, 2215.

72 M. Segala, Y. Takahata and D. P. Chong, *J. Electron Spectrosc. Relat. Phenom.*, 2006, **151**, 9–13.

73 D. P. Chong, *J. Chem. Phys.*, 1995, **103**, 1842–1845.

74 D. P. Chong, O. V. Gritsenko and E. J. Baerends, *J. Chem. Phys.*, 2002, **116**, 1760–1772.

75 J. M. Kahk, G. S. Michelitsch, R. J. Maurer, K. Reuter and J. Lischner, *J. Phys. Chem. Lett.*, 2021, **12**, 9353–9359.

76 A. T. Gilbert, N. A. Besley and P. M. Gill, *J. Phys. Chem. A*, 2008, **112**, 13164–13171.

77 D. Hait and M. Head-Gordon, *J. Chem. Theory Comput.*, 2020, **16**, 1699–1710.

78 J. M. Kahk and J. Lischner, *J. Chem. Theory Comput.*, 2023, **19**, 3276–3283.

79 G. Makov and M. C. Payne, *Phys. Rev. B: Condens. Matter Mater. Phys.*, 1995, **51**, 4014.

80 M. S. Hossain, G. S. Dhillon, L. Liu, A. Sridhar, E. J. Hiennnadi, J. Hong, S. R. Bare, H. Xin, T. Ericson and A. Cozzolino, *et al.*, *Chem. Eng. J.*, 2023, **475**, 146096.

81 V. Van Speybroeck, K. Hemelsoet, L. Joos, M. Waroquier, R. G. Bell and C. R. A. Catlow, *Chem. Soc. Rev.*, 2015, **44**, 7044–7111.

82 S. Kim, M.-S. Lee, D. M. Camaiioni, O. Y. Gutiérrez, V.-A. Glezakou, N. Govind, T. Huthwelker, R. Zhao, R. Rousseau and J. L. Fulton, *et al.*, *J. Am. Chem. Soc. Au*, 2023, **3**, 2487–2497.

83 A. M. Jubb, W. Hua and H. C. Allen, *Acc. Chem. Res.*, 2012, **45**, 110–119.

84 A. M. Prophet, K. Polley, G. J. Van Berk, D. T. Limmer and K. R. Wilson, *Chem. Sci.*, 2024, **15**, 736–756.

85 C. Weeraratna, C. Amarasinghe, W. Lu and M. Ahmed, *J. Phys. Chem. Lett.*, 2021, **12**, 5503–5511.

86 T. L. Tarbuck and G. L. Richmond, *J. Am. Chem. Soc.*, 2006, **128**, 3256–3267.

87 L. Onsager and N. N. Samaras, *J. Chem. Phys.*, 1934, **2**, 528–536.

88 S. W. Devlin, S. Jamnuch, Q. Xu, A. A. Chen, J. Qian, T. A. Pascal and R. J. Saykally, *J. Am. Chem. Soc.*, 2023, **145**, 22384–22393.

89 R. K. Lam, J. W. Smith, A. M. Rizzuto, O. Karslioğlu, H. Bluhm and R. J. Saykally, *J. Chem. Phys.*, 2017, **146**, 094703.

90 R. A. Kerr, *Science*, 2007, **316**, 188–190.

91 C. B. Field and V. R. Barros, *Climate change 2014–Impacts, adaptation and vulnerability: Regional aspects*, Cambridge University Press, Cambridge, 2014.

92 A. Rafiee, K. R. Khalilpour, D. Milani and M. Panahi, *J. Environ. Chem. Eng.*, 2018, **6**, 5771–5794.

93 D. W. Keith, *Science*, 2009, **325**, 1654–1655.

94 D. M. Glenna, A. Jana, Q. Xu, Y. Wang, Y. Meng, Y. Yang, M. Neupane, L. Wang, H. Zhao and J. Qian, *et al.*, *J. Phys. Chem. Lett.*, 2023, **14**, 10693–10699.

95 T. M. McDonald, J. A. Mason, X. Kong, E. D. Bloch, D. Gygi, A. Dani, V. Crocella, F. Giordanino, S. O. Odoh and W. S. Drisdell, *et al.*, *Nature*, 2015, **519**, 303–308.

96 Y. A. Wang and E. A. Carter, *Theoretical methods in condensed phase chemistry*, 2000, **vol. 5**, pp. 117–184.

97 M. Chen, X.-W. Jiang, H. Zhuang, L.-W. Wang and E. A. Carter, *J. Chem. Theory Comput.*, 2016, **12**, 2950–2963.

98 V. V. Karasiev and S. B. Trickey, *Adv. Quantum Chem.*, Elsevier, 2015, vol. 71, pp. 221–245.

99 W. C. Witt, B. G. Del Rio, J. M. Dieterich and E. A. Carter, *J. Mater. Res.*, 2018, **33**, 777–795.

100 X. Shao, K. Jiang, W. Mi, A. Genova and M. Pavanello, *Wiley Interdiscip. Rev.: Comput. Mol. Sci.*, 2021, **11**, e1482.

101 V. Gavini, K. Bhattacharya and M. Ortiz, *J. Mech. Phys. Solids*, 2007, **55**, 697–718.

102 J.-D. Chai and J. D. Weeks, *Phys. Rev. B: Condens. Matter Mater. Phys.*, 2007, **75**, 205122.

103 J. Behler, *J. Chem. Phys.*, 2016, **145**, 170901.

104 C.-K. Skylaris, P. D. Haynes, A. A. Mostofi and M. C. Payne, *J. Chem. Phys.*, 2005, **122**, 084119.

105 J. C. Prentice, J. Aarons, J. C. Womack, A. E. Allen, L. Andrinopoulos, L. Anton, R. A. Bell, A. Bhandari, G. A. Bramley and R. J. Charlton, *et al.*, *J. Chem. Phys.*, 2020, **152**, 174111.

106 D. Bowler, R. Choudhury, M. Gillan and T. Miyazaki, *Phys. Status Solidi B*, 2006, **243**, 989–1000.

107 A. Nakata, J. S. Baker, S. Y. Mujahed, J. T. Poulton, S. Arapan, J. Lin, Z. Raza, S. Yadav, L. Truflandier and T. Miyazaki, *et al.*, *J. Chem. Phys.*, 2020, **152**, 164112.

108 S. Mohr, L. E. Ratcliff, L. Genovese, D. Caliste, P. Boulanger, S. Goedecker and T. Deutsch, *Phys. Chem. Chem. Phys.*, 2015, **17**, 31360–31370.

109 L. E. Ratcliff, W. Dawson, G. Fisicaro, D. Caliste, S. Mohr, A. Degomme, B. Videau, V. Cristiglio, M. Stella and M. D'alessandro, *et al.*, *J. Chem. Phys.*, 2020, **152**, 194110.

110 S. Atchley, C. Zimmer, J. Lange, D. Bernholdt, V. Melesse Vergara, T. Beck, M. Brim, R. Budiardja, S. Chandrasekaran, M. Eisenbach *et al.* Proceedings of the International Conference for High Performance Computing, Networking, Storage and Analysis, 2023, pp. 1–16.

111 A. Castro, H. Appel, M. Oliveira, C. A. Rozzi, X. Andrade, F. Lorenzen, M. A. Marques, E. Gross and A. Rubio, *Phys. Status Solidi B*, 2006, **243**, 2465–2488.

112 N. Tancogne-Dejean, M. J. Oliveira, X. Andrade, H. Appel, C. H. Borca, G. Le Breton, F. Buchholz, A. Castro, S. Corni and A. A. Correa, *et al.*, *J. Chem. Phys.*, 2020, **152**, 124119.

113 A. Sharma, A. Metere, P. Suryanarayana, L. Erlanson, E. Chow and J. E. Pask, *J. Chem. Phys.*, 2023, **158**, 204117.



114 K.-H. Liou, C. Yang and J. R. Chelikowsky, *Comput. Phys. Commun.*, 2020, **254**, 107330.

115 Y. Zhou, J. R. Chelikowsky and Y. Saad, *J. Comput. Phys.*, 2014, **274**, 770–782.

116 G. Schofield, J. R. Chelikowsky and Y. Saad, *Comput. Phys. Commun.*, 2012, **183**, 497–505.

117 A. Natan, A. Benjamini, D. Naveh, L. Kronik, M. L. Tiago, S. P. Beckman and J. R. Chelikowsky, *Phys. Rev. B: Condens. Matter Mater. Phys.*, 2008, **78**, 075109.

118 W. H. Press, *Numerical recipes: The art of scientific computing*, Cambridge University Press, Cambridge, 3rd edn, 2007.

119 V. Hernandez, J. Roman, A. Tomas and V. Vidal, *Universitat Politècnica De Valencia, SLEPs technical report STR-6*, 2009.

120 F. Rabbi, C. S. Daley, H. M. Aktulga and N. J. Wright, *International Workshop on Accelerator Programming Using Directives*, 2019, pp. 66–88.

121 A. H. Palser and D. E. Manolopoulos, *Phys. Rev. B: Condens. Matter Mater. Phys.*, 1998, **58**, 12704.

122 D. Bowler and M. Gillan, *Comput. Phys. Commun.*, 1999, **120**, 95–108.

123 L. Genovese, T. Deutsch, A. Neelov, S. Goedecker and G. Beylkin, *J. Chem. Phys.*, 2006, **125**, 074105.

124 L. Genovese, T. Deutsch and S. Goedecker, *J. Chem. Phys.*, 2007, **127**, 054704.

125 A. Cerioni, L. Genovese, A. Mirone and V. A. Sole, *J. Chem. Phys.*, 2012, **137**, 134108.

126 I. Duchemin and F. Gygi, *Comput. Phys. Commun.*, 2010, **181**, 855–860.

127 N. M. Boffi, M. Jain and A. Natan, *J. Chem. Theory Comput.*, 2016, **12**, 3614–3622.

128 X. Jing, A. Sharma, J. E. Pask and P. Suryanarayana, *arXiv*, 2025, preprint, arXiv:2501.16572, DOI: [10.48550/arXiv.2501.16572](https://doi.org/10.48550/arXiv.2501.16572).

129 V. Gavini, S. Baroni, V. Blum, D. R. Bowler, A. Buccheri, J. R. Chelikowsky, S. Das, W. Dawson, P. Delugas and M. Dogan, *et al.*, *Modell. Simul. Mater. Sci. Eng.*, 2023, **31**, 063301.

130 V. Blum, R. Asahi, J. Autschbach, C. Bannwarth, G. Bihlmayer, S. Blügel, L. A. Burns, T. D. Crawford, W. Dawson and W. A. de Jong, *et al.*, *Electron. Struct.*, 2024, **6**, 042501.

131 A. Gulans, S. Kontur, C. Meisenbichler, D. Nabok, P. Pavone, S. Rigamonti, S. Sagmeister, U. Werner and C. Draxl, *J. Phys.: Condens. Matter*, 2014, **26**, 363202.

132 M. Govoni and G. Galli, *J. Chem. Theory Comput.*, 2015, **11**, 2680–2696.

133 T. D. Kühne, M. Iannuzzi, M. Del Ben, V. V. Rybkin, P. Seewald, F. Stein, T. Laino, R. Z. Khalilullin, O. Schütt and F. Schiffmann, *et al.*, *J. Chem. Phys.*, 2020, **152**, 194103.

134 F. Gygi, *IBM J. Res. Dev.*, 2008, **52**, 137–144.

